Advanced Physics Research

ADVANCED PHYSICS RESEARCH Open Access

www.advphysicsres.com

RESEARCH ARTICLE OPEN ACCESS

Nanoscale Thermal Transport in $Bi_2(Te, Se)_3$ Thermoelectric Material Using Pulsed STEM

Hyunyong Cho[1] | Hieu Duy Nguyen[1] | Isamu Yamada[2] | Koji Kimoto[1] | Takao Mori[3,4] | Naoyuki Kawamoto[1]

[1]Center for Basic Research on Materials, National Institute for Materials Science (NIMS), Tsukuba, Ibaraki, Japan | [2]Yamada R&D Support Enterprise, Ishioka, Ibaraki, Japan | [3]Research Center for Materials Nanoarchitectonics (MANA), National Institute for Materials Science (NIMS), Tsukuba, Ibaraki, Japan | [4]Graduate School of Pure and Applied Science, University of Tsukuba, Tsukuba, Ibaraki, Japan

Correspondence: Hyunyong Cho (cho.hyunyong@nims.go.jp) | Naoyuki Kawamoto (kawamoto.naoyuki@nims.go.jp)

Received: 9 February 2026 | **Revised:** 7 May 2026 | **Accepted:** 14 May 2026

Keywords: anisotropy | $Bi_2(Te, Se)_3$ | p-STAM technique | thermal boundary resistance | thermal diffusivity | thermal wave

ABSTRACT

Understanding thermal transport properties at the nanoscale can provide strategies for efficiently managing heat or improving energy conversion efficiency in various applications. Furthermore, when thermal paths can be traced and imaged at the nanoscale, materials or electronic devices can be designed to minimize heat loss. The demand for these technologies continues to grow rapidly. Here, we demonstrate imaging of thermal propagation in thermoelectric material ($Bi_2(Te, Se)_3$) using a spatially resolved technique that uses thermal waves induced by a pulsed convergent electron beam in a scanning transmission electron microscopy (STEM) mode at room temperature. The measurements with nanoscale clearly reveal the anisotropy inherent in $Bi_2(Te, Se)_3$ by quantifying the relative values of phase delay at each irradiated position. Also, the thermal wave propagation is significantly sensitive to the directions of the media, as if the heat carriers lose their memory of the vibration mode in each direction and switch to a new mode. Capturing various thermal properties, such as directional thermal pathways, from nanoscale imaging can provide a deeper understanding of how materials affect heat transport. This insight plays a vital role in designing materials for thermal management and energy conversion devices.

1 | Introduction

As modern electronic devices continue to shrink and operate under increasingly demanding thermal conditions, heat-related degradation has emerged as one of the leading causes of device failure. Thermal management has become a critical consideration in the design of materials and electronic devices. For example, nanoscale defects such as grain boundaries, which act to increase thermal resistance, can adversely affect the heat-sinking components within thermal management systems [1]. Thus, effectively managing heat at the nanoscale is no longer a secondary consideration; it can be central to the reliable operation and design of thermoelectric, microelectronic, and photonic systems. Despite the growing demand for such thermal management, precise thermal measurements with nanoscale spatial resolution remain a formidable challenge.

Traditionally, thermal transport properties have been evaluated using a variety of methods, including Raman spectroscopy [2, 3], time/frequency domain thermoreflectance (TDTR/ FDTR) [4–10], scanning thermal microscopy (SThM) [11–14], scanning near-field optical microscopy [15, 16]. Although these techniques have offered valuable insight into thermal transport phenomena, they often suffer from critical limitations, such as limited spatial resolution for nanoscale measurements (e.g., micrometer-scale spatial resolution for the TDTR technique) and confinement to surface sensitivity. In response to these limitations, the use of a focused electron beam with a transmission electron microscope

(TEM) has been proposed as a nanoscale heat source [17–19]. Recent advances using electron energy loss spectroscopy (EELS) have enabled temperature mapping by tracking shifts in plasmon peaks or phonon modes, offering sub-10 meV energy resolution without damaging the specimen [20–25]. However, these techniques still face challenges in detecting subtle temperature gradients [23], especially thermally sensitive and anisotropic materials. Furthermore, the lack of directional sensitivity of the current measurement schemes can make it difficult to investigate anisotropic thermal transport, one of the key properties of many layered materials.

In our previous studies, in a nanocomposite material, we demonstrated the direct measurement of a subtle temperature change caused by the electron beam in a TEM using a nanoscale thermocouple [26, 27]. More recently, we extended this approach by employing a pulsed electron beam periodically blanked by an electrostatic dose modulator (EDM) in scanning transmission electron microscopy (STEM) mode as a heat source [28]. By characterizing the phase delay and amplitude of the resulting thermal waves, we successfully extracted effective thermal diffusivity values of the sapphire (with a spatial resolution of ~10 nm). Additionally, phonon scattering at grain boundaries was directly visualized in polycrystalline AlN, demonstrating the technique's capability to uncover nanoscale thermal transport mechanisms. However, the materials used in our previous studies, while suitable for validating the methodology, showed weak thermal anisotropy with anisotropy ratio values of around 1.1 or less [29, 30]. To better demonstrate the capability of this pulsed STEM-based thermal analytical microscopy (p-STAM) technique, we identified the need to investigate materials with intrinsically stronger anisotropic thermal transport properties. Such measurements are not only scientifically significant but can also be critical for evaluating the directional sensitivity and spatial resolution of our technique.

In this study, we investigate the nanoscale thermal transport behavior of microfabricated n-type $Bi_2Te_{2.7}Se_{0.3}$ specimens (two-grain and multi-grain configurations), a well-known anisotropic thermoelectric material, by applying the p-STAM technique. By scanning a pulsed convergent electron beam across the specimens in STEM mode, we simultaneously acquire high-angle annular dark-field (HAADF) images and maps of the phase delay and the amplitude of thermal waves with nanometer-scale resolution. In the two-grain specimen, the phase delay of thermal waves varied with the direction of the heat flow, clearly showing the anisotropic nature of thermal transport. In the multi-grain specimen containing Te-rich secondary phase, the smaller average grain size compared to the two-grain specimen exhibited a reduced effective thermal diffusivity. Notably, a discontinuity (i.e., a nonlinear relationship) appears in the phase delay line profile at the interface between the secondary phase and the main matrix. This is attributed to being closely related to thermal resistance due to phenomena such as heat accumulation at the interface. These findings not only demonstrate the capability of the p-STAM technique for high-resolution thermal characterization but also provide new insights into the influence of grain structure and secondary phases in thermoelectric materials.

2 | Theoretical Framework for Thermal Wave Analysis

This section describes the theoretical framework used for the quantitative determination of the phase delay and amplitude characteristics of thermal waves, based on established thermal characterization methodologies. Specifically, the analytical approach originally developed by Ångstrom for measuring thermal conductivity is adapted to interpret the propagation behavior of thermal waves induced by periodic electron beam heating. [31] In this technique, one end of a long, thin thermal conductor is periodically heated, and the resulting thermal waves are monitored at a downstream location. A key advantage of this method is that it allows the extraction of thermal diffusivity without requiring prior knowledge of the specimen thickness. Figure 1 illustrates our experimental setup in this study. A focused pulsed electron beam serves as a nanoscale heat source within the TEM, enabling localized thermal excitation of the specimen. A nanoscale thermocouple, fabricated from sharpened constantan and chromel tips placed in direct contact with the specimen, was used to detect the propagation of the generated thermal waves. The principle is straightforward: by measuring the phase delay (i.e., how much the thermal wave slows down) and the amplitude decay (i.e., how much it diminishes in intensity), thermal transport properties can be characterized with nanometer-scale spatial resolution, as illustrated in Figure 1.

In this configuration, the difference between the original and delayed thermal waves is only known at the two ends (heating and thermocouple point). Because these two points are aligned along a straight path regardless of the geometry in between, a simplified 1D model can be employed to describe thermal wave propagation:

$$\frac{d^2T(x,t)}{dx^2} = \frac{1}{\alpha}\frac{dT(x,t)}{dt} \tag{1}$$

where T is the temperature, α is the thermal diffusivity, x is the distance, and t is the time. It should be noted that this formulation does not aim to describe the full radially symmetric temperature field generated near the electron-beam irradiation point, but instead provides an effective 1D description of thermal-wave propagation along the measurement path between the heating position and the thermocouple junction. Since the experiment is conducted at room temperature with modest electron-beam-induced temperature variations, radiative heat loss, which scales as T^4 and primarily affects the amplitude rather than the phase of the thermal response, is negligible. Convective heat loss is absent due to the high-vacuum environment ($\sim 2 \times 10^{-5}$ Pa) of the TEM column.

The periodic heat source is generated by an electron beam blanking system driven by a square pulse train with a tunable modulation frequency of up to 500 kHz. This focused electron beam delivers a time-dependent heat flux, $Q(t)$, to the specimen. When the beam is unblanked, $Q(t) = Q_0$; when blanked, $Q(t) = 0$. The beam switching time is extremely short (< 20 ns), ensuring that the square waveform of the heat pulse remains nearly ideal.

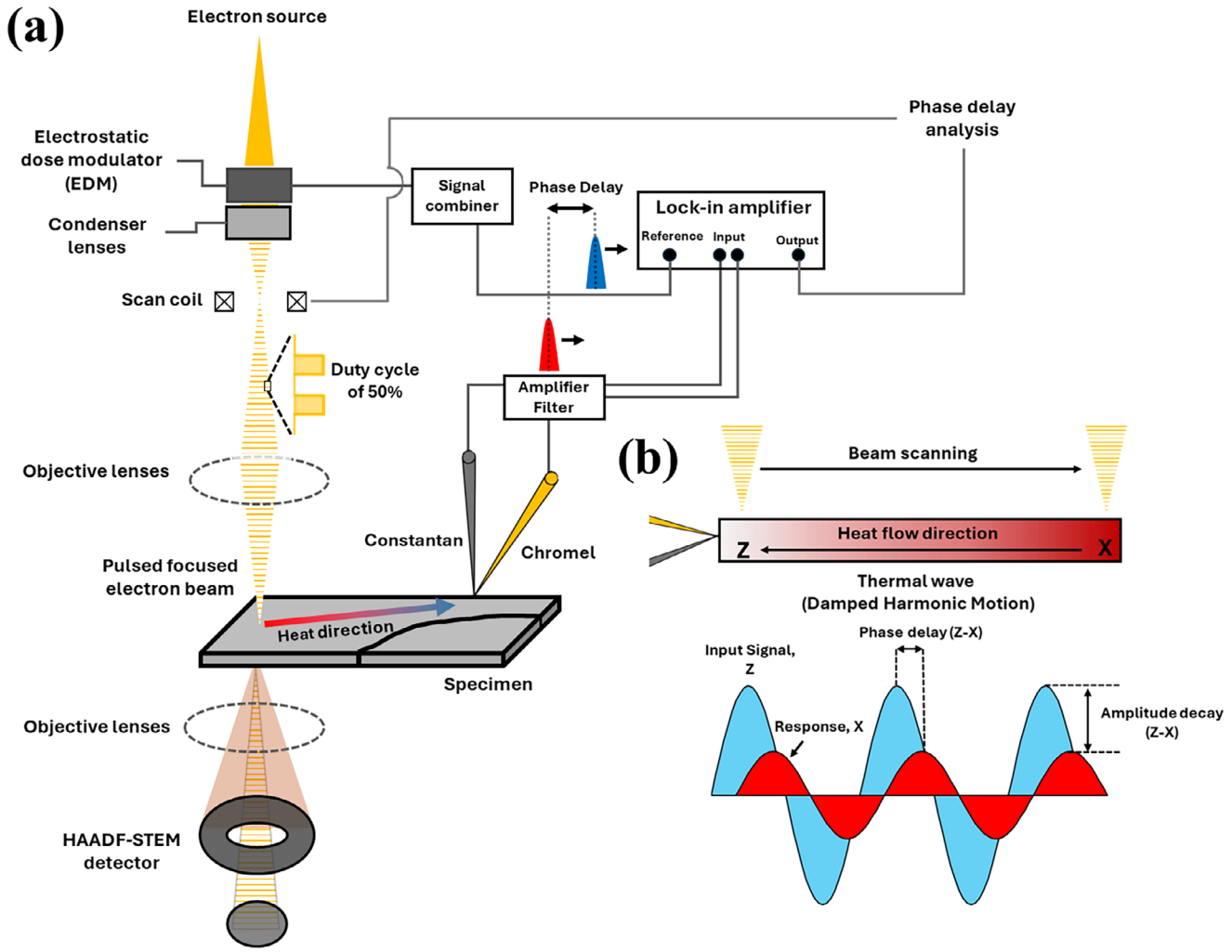

FIGURE 1 | (a) Illustration of the spatially resolved pulsed STEM-based thermal analytical microscopy (p-STAM) technique, where the heat is injected by a convergent electron beam under STEM, and the electron beam is modulated with a duty cycle of 50% under all conditions by an electrostatic dose modulator (EDM). The phase delay and amplitude of AC thermal waves at each position irradiated by the electron beam were acquired by lock-in amplifier. (b) Schematic diagram illustrating the propagation of thermal waves during beam scanning, showing the attenuation of signal amplitude and phase delay as a function of distance, compared to the input signal.

The Fourier transform of this heat flux is given by [32].

$$Q(t) = Q_0\left[\frac{1}{2} + \sum_{\substack{n=-\infty \\ n\neq 0}}^{\infty}\left|\frac{\sin\left(\frac{n\pi}{2}\right)}{n\pi}\right| . \exp\left\{i\left(n\omega t - \frac{n\pi}{2}\right)\right\}\right] \tag{2}$$

where $\omega = 2\pi f$ is the angular modulation frequency. It is important to note that a 50% duty cycle was consistently maintained throughout this study. Q_0 represents the total heat flux induced by the convergent electron beam and is estimated as bellows:

$$Q_0 = \frac{1}{A} \times P = \frac{1}{A} \times \left(\frac{\pi r_0^2 J}{e}\frac{\Delta E}{\Lambda} t\right) \tag{3}$$

where A is the cross-sectional area of the specimen, P is the power associated with the electron beam's heating effect on the specimen, assuming that mainly plasmon energy loss (ΔE) with an electron mean free path (Λ) contributes to heat generation. In addition, r_0 is the electron beam radius, J is the current density, e is the elementary charge, and t is the specimen thickness. In this study, since the specimen exhibited approximately uniform width and thickness within the entire region of interest, A was treated as constant to enable an effective 1D phase-delay analysis. By solving Equation (1) for each nth order and assuming a linear superposition of thermal waves, [28, 32] the following solution is obtained:

$$T(x,t) = \frac{Q_0}{\rho C_p \sqrt{\alpha}} \sum_{\substack{n=-\infty \\ n\neq 0}}^{\infty}\left|\frac{\sin\left(\frac{n\pi}{2}\right)}{n\pi}\right| \sqrt{\frac{1}{2|n|\pi f}} \exp \times\left(-\sqrt{\frac{|n|\pi f}{\alpha}}x\right) \exp\left[i\left(n\omega t - \sqrt{\frac{|n|\pi f}{\alpha}}x - \frac{\pi}{4} - \frac{n\pi}{2}\right)\right] \tag{4}$$

Herein, ρ denotes the material density, and C_p is the specific heat capacity. The derived solution is expressed as a complex

number, where the modulus corresponds to the amplitude and the argument corresponds to the phase of the thermal wave. The amplitude of the thermal wave as it propagates through the specimen is given by:

$$Amp(x) = \frac{Q_0}{\rho C_p \sqrt{\alpha}} \sum_{\substack{n=-\infty \\ n \neq 0}}^{\infty} \left| \frac{\sin\left(\frac{n\pi}{2}\right)}{n\pi} \right| \sqrt{\frac{1}{2|n|\pi f}} \times \exp\left(-\sqrt{\frac{|n|\pi f}{\alpha}} x\right) \quad (5)$$

This expression describes the exponential decay of thermal wave amplitude with distance, governed by both material properties and modulated frequency. Deviations from this ideal behavior in experimental measurements may indicate variations in specimen geometry, thermal boundary conditions, or local specific heat capacity.

Although the temperature response can be formally expressed as a harmonic series, the subsequent phase-delay analysis is restricted to the first harmonic component ($n = 1$), which dominates the detected signal due to the rapid attenuation of higher-order harmonics. Accordingly, the specimen's thermal diffusivity (α) can be directly determined from the spatial difference in phase delay measured at two distinct spatial positions, expressed as:

$$\Delta\theta = \theta_1 - \theta_2 = \sqrt{\frac{\pi f}{\alpha}} (x_2 - x_1) \quad (6)$$

where θ_1 and θ_2 are the phase delays of thermal waves measured at distances x_1 and x_2, respectively. In this study, this reference point was consistently selected to be in close proximity to the thermal junction between the specimen and the thermocouple. This linear relationship enables direct extraction of the thermal diffusivity by analyzing the spatial gradient of the measured phase delay, providing a thickness-independent evaluation of thermal transport properties. In this context, the extracted thermal diffusivity represents a local transport parameter derived from the thermal-wave phase delay. Because this phase-based analysis primarily reflects the thermal diffusion time scale, the resulting diffusivity is significantly less sensitive to geometric heat-spreading effects and instead captures the localized thermal transport behavior inherent to the nanoscale experimental configuration. It should be noted that Equations (1–6) are not intended to constitute a full forward model of the scanning thermal-wave experiment with a moving heat source. Instead, they provide an effective local description of the periodically modulated temperature field under harmonic excitation. In the present scanning configuration, the measured phase and amplitude at each position can therefore be interpreted as a quasi-local thermal response, and the analytical formulation is used as an interpretative framework to relate local phase evolution to intrinsic thermal transport properties and interfacial impedance. It must be emphasized that the analytical framework presented in Equations (1–6) constitutes a numerically simplified, first-order approximation of the full thermal-wave problem. The actual experimental geometry is governed by the heat equation in cylindrical coordinates, involving radial, angular, and depth-dependent terms. In the present treatment, only the dominant radial dependence of heat propagation is considered, while angular (θ) and depth (z) contributions are neglected. While this simplification enables tractable analytical extraction of thermal transport parameters, it may introduce numerical deviations whose magnitude depends on modulation frequency, thermal anisotropy, and boundary conditions. The extracted values should therefore be interpreted as effective first-order estimates. In addition, under the experimental conditions, the thermal diffusion length $L = \sqrt{(\alpha/\pi f)}$ is estimated to be approximately 2-6 μm at modulation frequencies of 10–60 kHz, assuming a thermal diffusivity on the order of 10^{-6} m^2 s^{-1} [33, 34]. This length scale is significantly larger than both the STEM scan pixel size (~30–60 nm) and the specimen thickness (~ 200–300 nm). Consequently, the temperature field varies smoothly over multiple scan pixels, allowing the moving electron beam excitation to be approximated as a sequence of local periodic heat sources.

According to Equation (6), the phase is expected to vary linearly with distance. While this assumption holds for homogeneous materials such as single crystals, deviations from linear phase behavior can arise in practical materials due to microstructural heterogeneity and interfacial effects. Identifying and interpreting such nonlinear deviations is essential for understanding the thermal transport behavior in real systems. In the following sections, we present a detailed analysis of the thermal diffusivity of n-type $Bi_2Te_{2.7}Se_{0.3}$ specimens (two-grain and multi-grain), a known anisotropic thermoelectric material, and further discuss the nonlinear phase delay trends that emerge due to embedded microstructures and anisotropic heat transport.

3 | Results and Discussion

3.1 | Thermal Waves Analysis and Microstructural Characterization of a Two-Grain $Bi_2Te_{2.7}Se_{0.3}$ Specimen

Figure 2 shows an HAADF-STEM image and energy dispersive X-ray spectroscopy (EDS) elemental maps of the two-grain specimen. The specimen was extracted from the bulk material and shaped using a focused ion beam (FIB) system, resulting in dimensions of approximately 7 μm × 10 μm and a thickness of ~200–300 nm. The HAADF-STEM image reveals a curved line exhibiting a discontinuous contrast variation from the lower left to the upper central region, corresponding to a grain boundary. In contrast, a region of slightly darker contrast is observed near the top of the image, which becomes more apparent in the EDS maps. Figure S1c shows a scanning electron microscope (SEM) image of the specimen during the FIB process, clearly indicating the presence of a single grain boundary. In addition, the bright-field (BF) TEM image reconstructed from multiple tiled frames (Figure S1d) confirms a grain boundary traversing the central part of the specimen. The darker region mentioned above is visible in the BF-TEM image and is likely attributed to local variations in specimen thickness. The relative specimen thickness, estimated from the ratio of the zero-loss peak to the total intensity in electron energy-loss spectroscopy (EELS) spectra, was evaluated at several locations across the specimen, as shown in Figure S2. Compared to points B and C, the relative thickness at point A (within the darker BF-TEM region) was found to be ~1.3 times greater, indicating a localized increase in thickness. The EDS

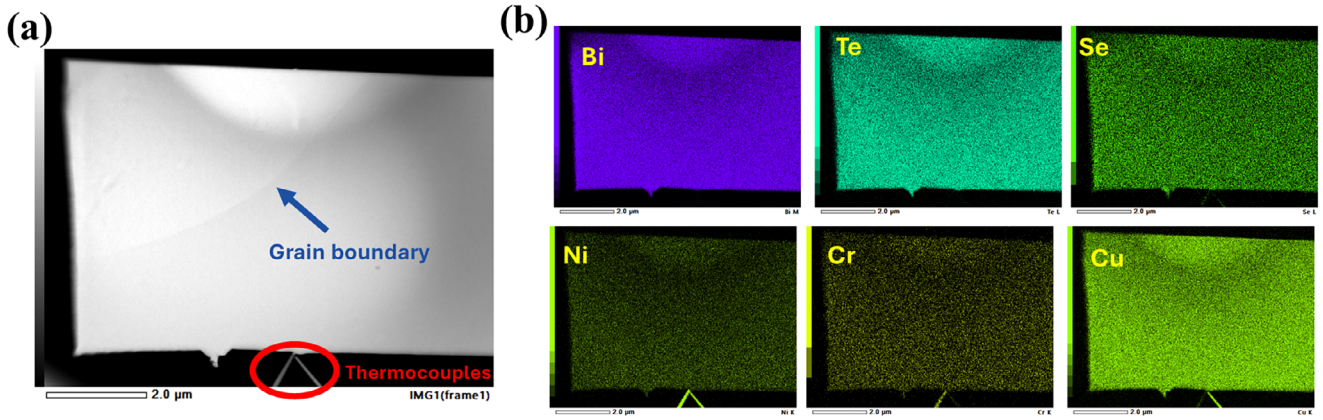

FIGURE 2 | (a) The HAADF-STEM image and (b) EDS result of the two-grain specimen. Thermocouples are in physical contact with the specimen and are indicated by red circles in the HAADF-STEM image.

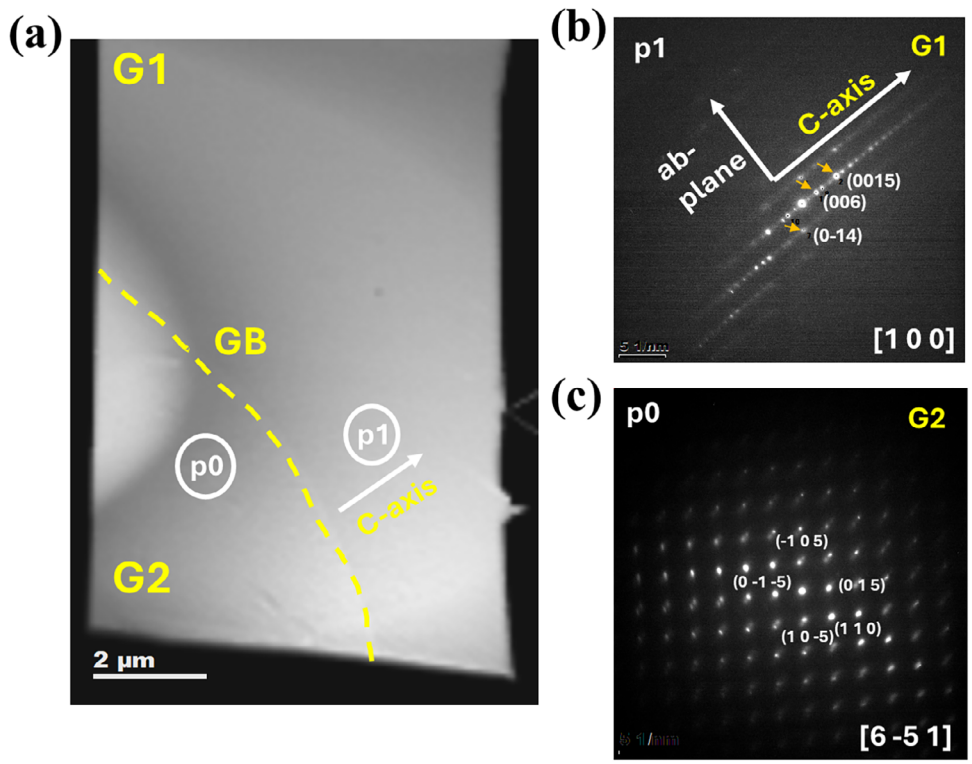

FIGURE 3 | (a) HAADF-STEM image of the two-grain specimen. G1 and G2 denote the grains located at the top and bottom corners of the HAADF-STEM image, respectively. The grain boundary is marked with a yellow dashed line. Selected area electron diffraction patterns obtained at positions p1 (b) and p0 (c), illustrating local crystallographic information.

elemental maps in Figure 2 also clearly demonstrate that the nanoscale thermocouple, composed of constantan (Ni-Cu) and chromel (Ni-Cr), are in direct physical contact with the specimen at the bottom of the image.

Figure 3 presents an HAADF-STEM image and selected area electron diffraction (SAED) patterns acquired at two points (p0 and p1) of the specimen. The yellow dashed line denotes the grain boundary, which clearly separates grain 1 (G1) and grain 2 (G2). Based on the SAED pattern, the zone axis of G1 was identified to lie along the [1 0 0] crystallographic direction. As shown in Figure 3b, the *c*-axis orientation is inclined diagonally. Notably, the *c*-axis in G1 is aligned in the direction indicated by the white arrow in the real-space image (Figure 3a). This arrow corresponds to the direction in which the thermocouples are physically positioned in the experimental setup. This spatial alignment suggests that the atomic layers of $Bi_2Te_{2.7}Se_{0.3}$ in G1 are stacked along the direction of the thermocouples, potentially revealing a link between the crystallographic orientation and the direction of the heat transport. Bismuth telluride (Bi_2Te_3), a widely studied thermoelectric material, possesses a layered structure composed of Te-Bi-Te-Bi-Te quintuple layers stacked

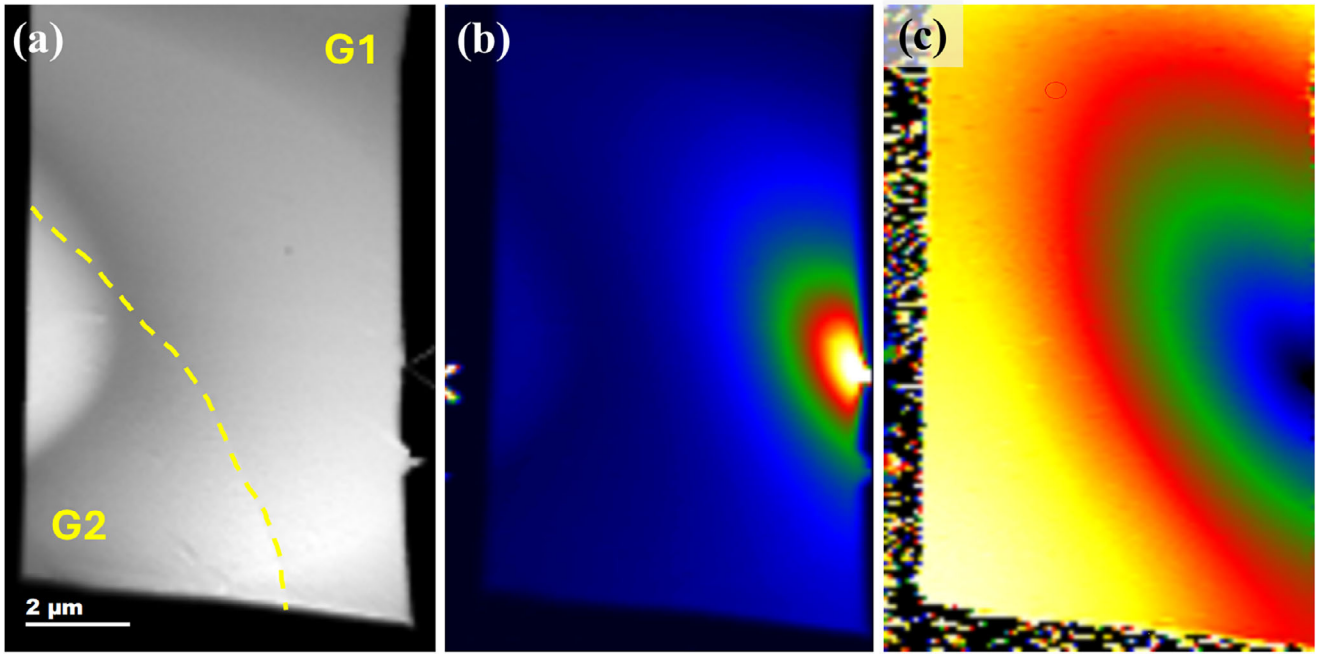

FIGURE 4 | (a) HAADF-STEM image of the two-grain specimen, (b) thermal wave amplitude distribution, and (c) corresponding phase delay map acquired at a modulation frequency of 38 kHz, illustrating spatial variations in thermal response.

along the *c*-axis via van der Waals interactions [35]. Due to this layered nature, both electrical and thermal conductivity are anisotropic, exhibiting significantly higher values along the ab-plane than along the *c*-axis. This anisotropy implies that thermal transport along the arrow direction (parallel to the *c*-axis in Figure 3a) is relatively suppressed compared to the direction perpendicular direction. In contrast, the SAED pattern of G2 was indexed to a zone axis of [6 $\bar{5}$ 1] as shown in Figure 3c), confirming that G1 and G2 exhibit distinct crystallographic orientations.

Amplitude and phase delay maps of the two-grain specimen were acquired at various modulated frequencies using the p-STAM technique. Figure 4 and Figure S3 display the corresponding HAADF-STEM images along with thermal wave amplitude and phase delay maps at modulation frequencies of 38, 20, and 30 kHz, respectively. Interestingly, in the G1 region, both amplitude and phase delay maps clearly reveal an ellipsoidal rather than radial thermal wavefront, indicating pronounced anisotropic thermal propagation. This observation strongly supports the interpretation that the anisotropy inferred from the SAED pattern is well aligned with the crystallographic orientation of the grain. Moreover, the spatial variations in phase delay within G1 indicate that thermal wave propagation is highly sensitive to local crystallographic orientation, even at nanometer-scale spatial resolution determined by the scan step size. In contrast, thermal wave behavior in G2 exhibits a markedly different morphology, which can be attributed to the differing crystal orientations relative to G1. This behavior may also provide insight into the crystallographic plane along which heat is conducted, given the slow thermal waves are transferred in the G2 system compared to the fast direction (ab-plane of the crystal) observed in G1 (as will be discussed in detail later).

According to Equation (6), the local thermal diffusivity can be quantitatively determined from the gradient of the phase delay, assuming a contrast modulation frequency. Figure 5b–d presents the phase delay line profiles (corresponding to the map in Figure 5a) along different directions at various modulated frequencies. In particular, within G1, the *Z-Y* and *Z-X* directions correspond to the ab-plane and the *c*-axis of the crystal orientation, respectively. A clear correlation is observed between the phase delay gradients and the modulation frequencies of the pulsed convergent electron beam: as the frequency increases, the phase gradient steepens, consistent with Equation (6). Along the *Z-Y* direction (Figure 5b), the phase delay increases linearly with distance. In contrast, along the *Z-M* and *Z-X* directions (Figure 5c,d), which cross the grain boundary, the phase delay exhibits nonlinear behavior beyond the boundary, appearing as either a smooth curve or two linear segments with different slopes. This strongly suggests that the thermal diffusivities of the two grains differ according to the crystallographic direction, due to intrinsic thermal anisotropy. Therefore, phase gradients in each region must be evaluated to determine the corresponding thermal diffusivities. At a modulation frequency of 38 kHz, the phase slopes in the *Z-Y*, *Z-M'*, *M'-M*, *Z-X'* and *X'-X* directions are approximately 0.30, 0.52, 0.38, 0.6, and 0.37 rad/μm, respectively. In the G1region, the slope along the ab plane (*Z-Y*) is about half that along the *c*-axis (*Z-X'*), clearly indicating the anisotropy behavior. All profiles were fitted using linear approximation, excluding regions within ~1 μ*m* from the end of the specimen edge to avoid ballistic effects [36, 37] and thermal wave interference [38, 39] (see black dashed line in Figure 5b–d). Anisotropy is also evident in the amplitude profiles (Figure S4): the *Z-X* direction exhibits a more pronounced amplitude decay with distance than the *Z-Y* direction.

Figure 5e summarizes the average thermal diffusivity values estimated from Equation (6) for each region, with error bars indicating the associated uncertainties. The average thermal diffusivity along the *Z-Y* direction, corresponding to the *ab*-plane

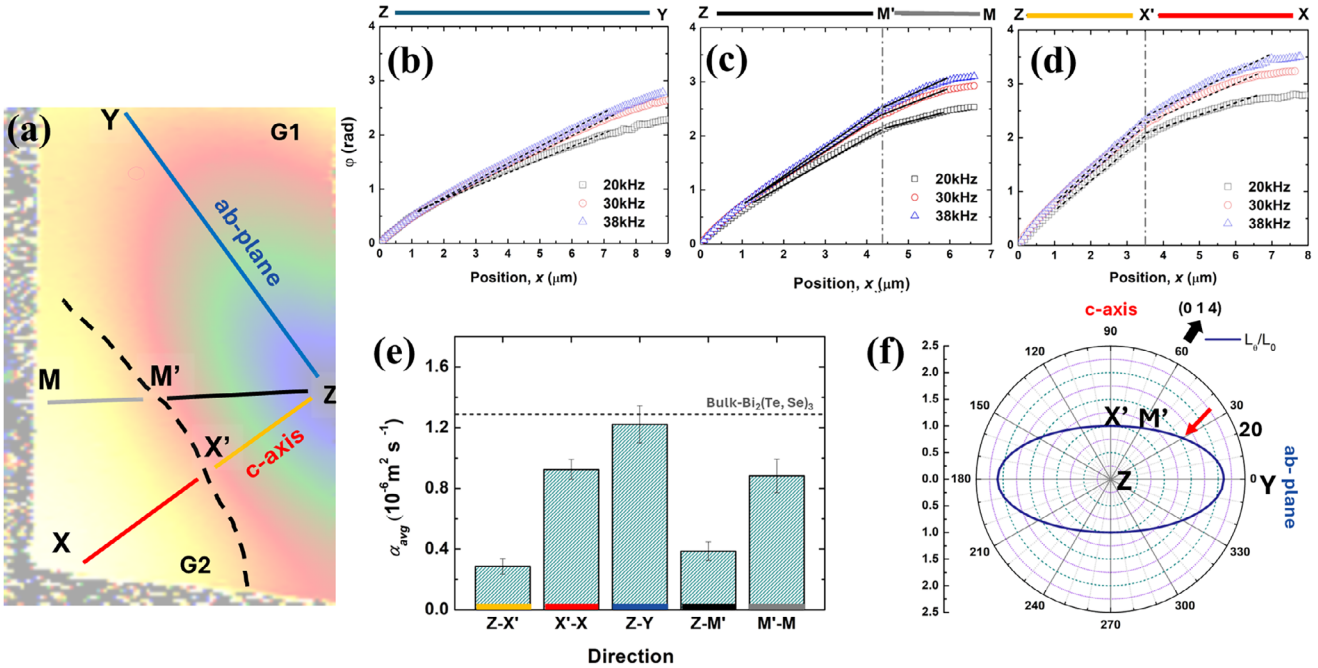

FIGURE 5 | (a) Blurred phase delay map highlighting the selected line profiles. The *Z-X'* direction aligns with the crystallographic *c*-axis, and the *Z-Y'* direction corresponds to the in-plane (*ab*-plane) direction of the system. (b–d) Phase delay profiles of thermal waves along *Z-Y*, *Z-M*, and *Z-X* directions at varying modulation frequencies (20, 30, 38 kHz). (e) Estimated average thermal diffusivities in each direction. Directional markers in the phase map are color-matched with the phase profiles and thermal diffusivity directions for visual consistency. The in-plane thermal diffusivity of the polycrystalline sample measured by a laser flash analyzer (LFA) is shown as a gray dashed line. (f) Elliptical representation in polar coordinates based on directional thermal diffusion lengths, providing a visual depiction of anisotropic thermal transport.

of the crystal, is approximately 1.2×10^{-6} m^2 s^{-1} — about 4 times higher than that along *Z-X'* (*c*-axis) (~0.29×10^{-6} m^2 s^{-1}). To quantify the directional thermal conductivities, the relation $\kappa = \alpha C_p \rho$ was employed, where C_p is the specific heat capacity, and ρ is the density. Bulk values of $C_p = 0.16\, J\, g^{-1}\, K^{-1}$, and $\rho = 7.7$ g m^{-3}, obtained from measurements of the same material were used in the calculation. The ab-plane thermal conductivity was ~ 1.47 W m^{-1} K^{-1}, while the *c*-axis value was significantly lower, at ~ 0.36 W m^{-1} K^{-1}. Prior studies have reported thermal-conductivity anisotropy ratio of 2–2.8 times for Bi_2Te_3-based system [29, 40, 41]. The larger anisotropy ratio observed here (~4) compared to typical bulk values (2–2.8) should be interpreted with caution. As a primary consideration, the present analysis is based on a numerically simplified first-order approximation, in which the angular curvature and depth-dependent terms of the full cylindrical Laplacian are neglected. This simplification introduces a systematic uncertainty in the extracted directional diffusivity values and may lead to an overestimation of the apparent anisotropy ratio. Without a full numerical treatment of these higher-order contributions, the magnitude of this effect cannot be quantitatively resolved. While this approximation likely accounts for a significant portion of the discrepancy, the larger ratio may also reflect intrinsic physical effects associated with nanoscale heat transport. As the dimensions are reduced from bulk to the nanoscale, the thermal conductivity can decrease at different rates depending on direction owing to the classical size effect [42, 43]. Because phonon transport in layered Bi_2Te_3 is intrinsically anisotropic, boundary scattering in nanoscale specimens can suppress the effective phonon mean free path in a direction-dependent manner, which may modify the apparent thermal anisotropy compared with bulk materials. In other words, specimen miniaturization can disproportionately limit the effective phonon mean free path, depending on transport direction, due to enhanced phonon scattering. Previous studies on layered van der Waals materials have shown that size-dependent boundary scattering can modify the apparent thermal anisotropy, suggesting that directional thermal transport may evolve nonuniformly as the characteristic length scale is reduced [44–48]. Along the ab-plane of a bulk single crystals, the thermal conductivity is typically ~2.2 W m^{-1} K^{-1} [40], whereas nanowires with diameters of 200 − 300 *nm* exhibit markedly lower values of 1.37 − 1.47 W m^{-1} K^{-1} [43, 49]. Assuming the same specific heat and material density as in our system, these literature values are consistent with the thermal diffusivity measured along the *Z-Y* direction (Figure 5e). Directly measuring the thermal conductivity of nanoscale samples along the *c*-axis is technically challenging in a layered structural system. Nevertheless, if the reduction in thermal diffusivity arising from the size effect corresponds to the value measured along the *c*-axis (*Z-X'*), this finding suggests that the rate of decrease in thermal diffusivity is inherently nonuniform compared to that along the ab-plane (*Z-Y*). As also shown in Figure 5e, the in-plane thermal diffusivity (perpendicular to the *c*-axis; gray dashed line) of a polycrystalline bulk specimen with grains naturally aligned during sintering process is comparable to, or slightly higher than, that along *Z-Y*. Additionally, the value along *Z-M'* is marginally higher than that along *Z-X'*, reflecting their angular offset. Taken together, while nanoscale physical effects may influence the observed anisotropy, the present results should primarily be interpreted as first-order estimates within the simplified analytical framework, and the

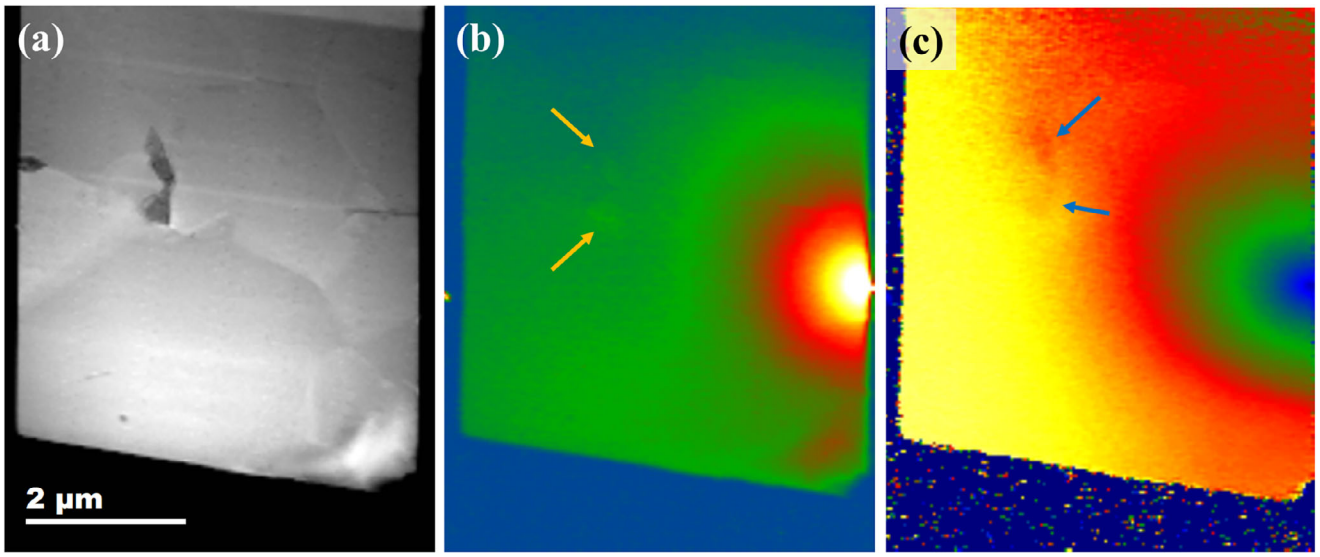

FIGURE 6 | (a) HAADF-STEM image of the multi-grain specimen containing Te-rich precipitates, (b) thermal wave amplitude distribution, and (c) corresponding phase delay map acquired at a modulation frequency of 60 kHz. The presence of precipitates influences both amplitude and phase delay, revealing localized variations in thermal wave propagation (indicated by yellow and blue arrows in the amplitude and phase delay maps, respectively).

relative contributions of analytical approximation and intrinsic physical mechanisms cannot be unambiguously separated.

To elucidate the anisotropy, we modeled the phase-delay map as an ellipse in polar coordinates using the thermal diffusion length $L = \sqrt{\alpha/\pi f}$, which is the reciprocal of the phase-delay gradient (Equation (6)). Normalizing spatial coordinates by the shortest diffusion length (i.e. along the *c*-axis) yields an elliptical distribution (Figure 5f). The major axis aligns with the in-plane crystallographic direction, whereas the minor axis corresponds to the *c*-axis. In real space, the angular difference between the *Z*-*X*' and *Z*-*M*' directions is ∼30°, indicating that *Z*-*M*' corresponds to the (0 1 4) crystallographic plane. This geometry implies an angular dependence of thermal diffusivity given by $\alpha_\theta = \alpha_c \times (L_\theta/L_c)^2$, linking directional diffusivity to crystal symmetry. θ and c denote the specific angles and *c*-axis direction of the crystal, respectively. This analytical framework extends to grain G2. For instance, when the thermal waves propagate along *Z*-*X* (Figure 5a), the propagation direction in G2 is identified as the [2 5 1], which forms an angle of ∼30° with the ab-plane. Applying the anisotropic thermal transport model then yields a directional diffusivity of $\sim 0.7 \times 10^{-6}$ m^2 s^{-1} along *X*'-*X*, slightly lower than the measured $\sim 0.9 \times 10^{-6}$ m^2 s^{-1}; closer agreement is obtained for an angular offset of ∼20°.

3.2 | Thermal Waves Analysis of a Multi-Grain $Bi_2Te_{2.7}Se_{0.3}$ Specimen

Figure 6 and Figure S5a–c show the HAADF-STEM images and corresponding amplitude and phase-delay maps of the multi-grain specimen at modulation frequencies of 60 and 20 kHz, respectively. The multi-grain specimen exhibits a slightly smaller grain size than the two-grain specimen, as shown in Figure 6a. The HAADF-STEM image reveals regions of darker contrast within the specimen, which are associated with secondary phases embedded in the matrix. To identify the origin of these darker-contrast regions, elemental distributions were investigated using EDS mapping. The results show that the dark regions correspond to Te-rich secondary phases embedded within the specimen, as depicted in Figure S5d. Compared to the previous observations (Figure 4; Figure S3), the amplitude and phase-delay distributions exhibit notable differences in thermal-wave behavior. In particular, the thermal wave propagation within the multi-grain region appears more isotropic, suggesting a change in thermal transport behavior arising from the random orientation of grains. In addition, distinct changes in both the amplitude and phase-delay maps are observed in the Te-rich regions, indicating locally anomalous thermal-wave behavior.

Figure 7 shows two red- and blue-dashed lines drawn across multiple grain boundaries (marked with the yellow lines) in the HAADF-STEM image (Figure 7a) and the corresponding phase line profiles (Figure 7b,c). The phase gradient in Figure 7b undergoes a sequence of changes, initially shallow, then steeper, and finally flattening as it passes through three individual grains. Although the random grain orientations render the overall propagation of thermal waves more isotropic, the individual grains retain their intrinsic anisotropic behavior, providing a clear example of localized thermal directionality. In addition, the phase-gradient variations observed in Figure 7c and Figure S6b highlight the spatial dependence of thermal behavior within each region, which is captured by the estimated thermal diffusivity shown in Figure S6c. Overall, the thermal diffusivity values of the multi-grain specimen largely fall within the range derived from the two-grain specimen: however, some values lie below the minimum observed in the two-grain specimen, suggesting that grain-size reduction may contribute to the decreased thermal diffusivity. The phase line profiles at 20 and 60 kHz (Figure 7b,c) also show a noticeable change in phase slope. Moreover, the phase profile of Line 4 exhibits a nonlinear trend with a sharp drop and jump near the Te-rich secondary phase region (L4-3). This effect is more pronounced at higher frequencies, likely due to the reduced thermal-wave diffusion length (L). In other

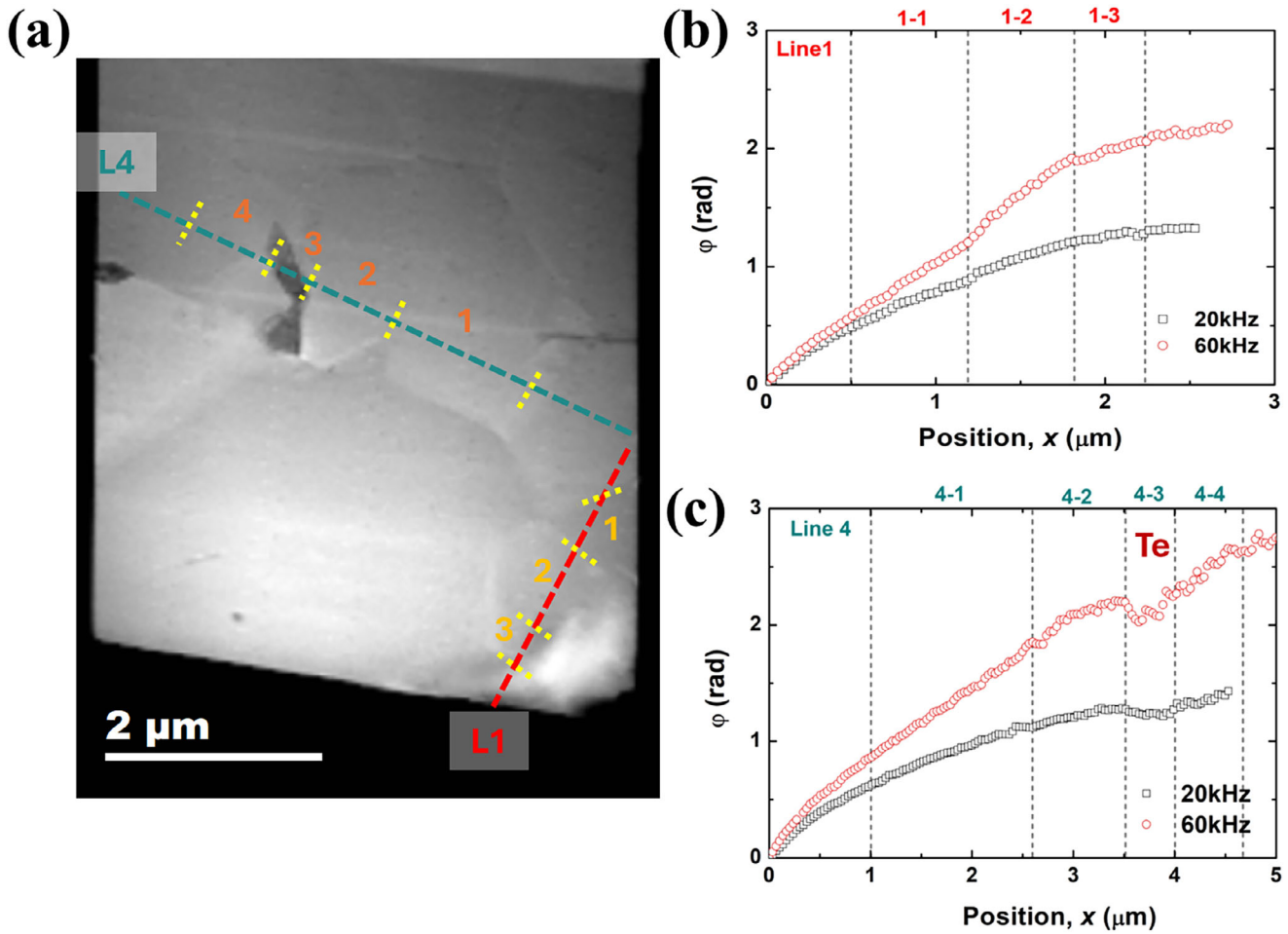

FIGURE 7 | (a) HAADF-STEM image of the multi-grain specimen, with the direction of the line profiles for phase delay analysis marked on the image. The grain boundaries are delineated by yellow dashed lines for visual clarity. Phase delay line profiles in Line 1 and Line 4 (L1 and L4) directions are presented in (b) and (c), corresponding to modulation frequencies of 20 and 60 kHz, respectively.

words, a shorter thermal diffusion length can improve spatial resolution, facilitating the detection of nanoscale features such as nano precipitates.

It is also instructive to further examine the nonlinear phenomena exhibiting a concave-down profile (Figure 7c; Figure S6b), as it may provide insight into underlying thermal transport mechanisms. Within a homogeneous medium, analyzing the nonlinearity of thermal-wave propagation requires consideration only of the thermal diffusivity of each grain in this system. In contrast, propagation through two different media may require additional consideration of differences in thermal properties and interfacial effects. In the presence of thermal impedance mismatch, the amplitude and phase of the periodically modulated temperature field can be modified at the interface, analogous to the reflection and transmission phenomena observed in conventional wave systems. This analogy provides a convenient framework for describing interfacial phase and amplitude modulation in thermal-wave measurements. Here, the reflection and transmission of the thermal wave can be determined by the thermal effusivities (e) of the two materials. Thermal effusivity quantifies a material's ability to exchange heat with its surroundings, defined as $e = \sqrt{\kappa \rho c_p}$, where κ is thermal conductivity, ρ is density, and $c_p$is the specific heat capacity. Assuming a normal incidence of the thermal wave onto the interface, with the wave propagating from Material 1 to Material 2, the reflection coefficient (r) and the transmission coefficient (t) are obtained from the continuity conditions of temperature and heat flux at the boundary, and are given by the following expression [39]:

$$r = \frac{e_1 - e_2}{e_1 + e_2} \tag{7}$$

$$t = \frac{2e_1}{e_1 + e_2} \tag{8}$$

where e_1 is the thermal effusivity of the incident medium (Material 1) and e_2 is the thermal effusivity of the second medium (Material 2). These coefficients describe how much of the thermal wave is reflected back into the first medium and how much is transmitted into the second, implying that the thermal-effusivity mismatch plays a critical role in governing the thermal-wave propagation at material interfaces, influencing both reflection and transmission. For instance, when a thermal wave propagates from a medium with high thermal effusivity, such as a metal inclusion, into a surrounding medium with significantly lower effusivity (i.e., $e_1 \gg e_2$), a strong mismatch occurs at the interface. A reflection coefficient of $r \approx +1$ indicates strong reflection, com-

monly referred to as the thermal-wave mirroring effect. While a transmission coefficient of $t \approx 2$ suggests that the temperature amplitude just across the interface (in Material 2) can be approximately twice that of the incident wave, it is crucial to note that the actual heat flux into the low-effusivity Material 2 remains very small due to its inherently low thermal effusivity. These reflection and transmission phenomena are direct results of the thermal impedance mismatch between the two materials. Furthermore, the thermal-wave mirroring effect at the interface leads to a localized enhancement of the harmonic temperature response within the high-effusivity region, with a reduced penetration of the periodically modulated thermal field into the low-effusivity medium. From this perspective, the downward-convex phase profile shown in Figure 7c and Figure S6c appears to be closely related to the nonlinear trend induced by the effusivity mismatch. In this context, the apparent phase drop and subsequent recovery reflect a localized modification of the phase response induced by thermal-impedance mismatch, rather than distinct physical mechanisms. By estimating the thermal conductivity, $\kappa = \alpha \cdot c_p \cdot \rho$, from the measured thermal-diffusivity values, the effusivity (e) can be approximately determined, on the basis of known density and specific heat capacity values for each bulk material. In the case of Line 4 in Figure 7c, the thermal-effusivity values for Te and its adjacent region (L4-2) are 2192 and 1287 $Ws^{1/2}\ m^{-2}\ K^{-1}$, respectively. The reflection coefficient, representing the ratio between the reflected and incident thermal wave amplitudes, is calculated to be approximately 0.26, indicating partial thermal-wave reflection at the interface. The reflected thermal wave can overlap with the incident wave originating from a moving heat source, leading to interference effects. This interference related to the thermal confinement, can induce nonlinear distortions in the phase profile, manifesting as sharp drops or jumps deviating from the expected linear behavior. Nonlinear behavior, including a phase jump, is not limited to the phase profile but also appears in the amplitude of thermal waves. Figure S7 shows that the attenuation of the thermal wave follows an exponential decay with distance, exhibits a rise near the Te region, and subsequently decreases again in the surrounding matrix. This consistent trend supports the presence of localized thermal interactions and wave modulation.

Furthermore, it is worth discussing that discontinuities—such as a phase jump—may be closely associated with the thermal resistance at the interface. As previously mentioned, these discontinuities can be interpreted as the result of contrasting thermal-energy accumulation and decay across the interface, which can be described in terms of thermal-wave reflection and transmission. Therefore, with knowledge of the material properties, a simple quantitative analytical model can be constructed to describe the thermal-wave discontinuities associated with thermal resistance in our measurement system (see the Supporting Information). To quantify the interfacial phase jump, we used an analytical model assuming a thermal-effusivity mismatch under the constraints of linear response, frequency-independent thermal parameters, and unidirectional heat propagation. As detailed in the Supplementary Information, the observed interfacial phase jump can be attributed to the thermal-effusivity mismatch or admittance mismatch at the boundary, which results in a frequency-dependent thermal phase delay. We derived that the interfacial phase jump is governed by the thermal boundary resistance (R_{TBR}), the effective thermal effusivity ($\frac{e_1 e_2}{e_1+e_2}$), and the frequency (ω) of the thermal wave, resulting in the following expression:

$$\Delta\Phi_{jump} \approx -R_{TBR} \cdot \frac{e_1 e_2}{e_1 + e_2} \cdot \sqrt{\frac{\omega}{2}} \tag{9}$$

In the equation representing the phase jump ($\Delta\Phi_{jump}$), the negative sign preceding the interfacial thermal resistance indicates a physical delay in the phase of the thermal wave. Using this model, it is possible to roughly estimate the R_{TBR} values at the interfaces corresponding to Line 3 and Line 4 (Figure S6b; Figure 7c). By estimating the $e_1 and\ e_2$ values and using the measured $\Delta\Phi_{jump}$values from each region, the R_{TBR} values can be approximately determined, assuming known values for the density and specific heat capacity of each bulk material. The estimated R_{TBR} values for Line 3 and Line 4 are approximately (3.0 ± 0.6) and (4.0 ± 0.8) × 10^{-7} $m^2\ K\ W^{-1}$, respectively. According to the literature [6, 7, 11], the grain-boundary resistance generally covers a range from ~ 10^{-9} $m^2\ K\ W^{-1}$ to about ~ 10^{-8} $m^2 K\ W^{-1}$. While the interfaces in the present system involve two materials with differing thermal properties, the calculated R_{TBR} values are on the order of ~ 10^{-7} $m^2 K\ W^{-1}$, which is somewhat higher than the grain-boundary resistance values commonly reported in literature. The interfaces investigated correspond to phase boundaries between the Bi_2Te_3 matrix and secondary phase with different thermal properties, where interfacial thermal resistance can become larger due to thermal property mismatch across the boundary [42]. This discrepancy reflects the simplified nature of the present analytical framework, which is intended to provide an effective, first-order description of interfacial phase behavior rather than a fully quantitative evaluation of absolute thermal boundary resistance. Nonetheless, the model can still offer valuable information regarding the relative thermal boundary resistance at interfaces. For instance, the $\Delta\Phi_{jump}$value measured in Line 4 exceeds that of Line 3, and this is accomplished by a higher thermal boundary resistance. This trend suggests that the phase jump can serve as an indicator of increasing thermal resistance across the interface. These findings demonstrate the potential of phase-based thermal wave analysis for characterizing interfacial thermal properties, even in systems with complex material boundaries.

4 | Conclusion

In this study, we employed a p-STAM technique to investigate nanoscale thermal transport in *n*-type $Bi_2Te_{2.7}Se_{0.3}$ specimens with well-defined microstructures, including two-grain and multi-grain configurations. Using a periodically modulated pulsed electron beam as a localized heat source and analyzing the resultant thermal-wave phase delay with nanometer-scale spatial resolution, together with complementary observations of amplitude attenuation, we successfully characterized directional thermal diffusivity and interfacial thermal behavior in highly anisotropic thermoelectric materials. In the $Bi_2Te_{2.7}Se_{0.3}$ two-grain specimen, strong anisotropy in thermal diffusivity was clearly observed, with in-plane (*ab*-plane) value exceeding out-of-plane (*c*-axis) transport by a factor of four. This anisotropy was also successfully visualized at the nanoscale in the phase delay map. A simplified elliptical representation in polar coordinates, constructed from directional thermal diffusion lengths inferred from the phase gradient, provided a visual depiction of

anisotropic heat flow and allowed rough estimation of thermal diffusivity in arbitrary directions. In the multi-grain specimen, reduced grain size led to more isotropic thermal behavior overall; however, individual grains retained their intrinsic anisotropy, highlighting localized thermal directionality within the material. Nonlinear thermal behavior was observed in both specimens. In particular, distinct nonlinearities in the thermal-wave phase—such as abrupt phase jumps or drops—were detected near inclusion/grain boundaries in the multi-grain specimen. These features were attributed to thermal-wave reflection and transmission, in an analogous sense, induced by mismatches in thermal effusivity. By introducing a simplified analytical model, we correlated the magnitude of the interfacial phase jumps with the thermal boundary resistance (R_{TBR}), yielding estimated values in the range of $\sim 3.0 - 4.0 \times 10^{-7}$ m^2 K W^{-1}. Application of this model enabled assessment of relative thermal boundary resistance at interfaces, offering useful insights into interfacial thermal transport properties. This study highlights the power of p-STAM to capture anisotropic heat flow and quantify interface resistance at the nanoscale. In addition, our results confirm that p-STAM can simultaneously capture thermal-transport properties, crystallographic orientation, and elemental mapping, thereby streamlining multimodal characterization within a single experiment. We believe that these insights are crucial for the thermal design of next-generation thermoelectric and heat-sensitive functional materials.

5 | Experimental Section

5.1 | Materials Synthesis

High-purity elements of Bi (99.99%), Te (99.99%), Se (99.99%) were directly weighed according to the nominal composition $Bi_2Te_{2.7}Se_{0.3}$, and then the stoichiometric mixture was loaded in an evacuated quartz ampoule. The sealed ampoules were heated at 1073K, maintained for 24 h, and then cooled slowly for 30 h in a furnace. The melted ingots were pulverized by hand grinding and mechanical ball milling for 3 h under an argon atmosphere. The powders produced by each method were directly loaded into a graphite die with a 12.7 mm diameter and then sintered by hot-press sintering at 773K for 1 h under a uniaxial pressure of 50 MPa.

5.2 | Preparation of Specimens

The specimens containing two grains and multi-grains were microfabricated using a FIB system (Hitachi Ethos NX-5000). Here, a sintered body made by hand grinding was used to fabricate a specimen containing only two grains, and the grain size of the specimens was observed to be approximately 6 μm or larger. The multi-grain specimen was fabricated using a ball-milled sintered body, and the grain size was observed to be approximately 2–3 μm. After microfabrication, each specimen was attached to a Cu attachment on a TEM holder. The two-grain specimen has dimensions of about 10 μm (length), about 7 μm (width) by 200 to 300 nm (thickness), and the multi-grain specimen has dimensions of about 8 μm (length), about 5 μm (width), and by ~200 to 300 nm (thickness).

5.3 | Characterizations

Electron microscopy measurements were performed using a JEOL JEM-3100FEF TEM operating at 300 kV and equipped with an electrostatic dose modulation (EDM basic) system by JEOL to generate a pulsed electron beam. The system operated in STEM mode, utilizing a 70 μm condenser lens aperture, with a beam convergence semi-angle of approximately 6.8 mrad. The electron beam had an effective size of around 2-3 nm and a beam current of ~0.5 nA under standard settings, while enhanced beam current settings allowed for ~1.4 nA (for details, see in Ref. [28]). Beam scanning in STEM mode was controlled via a Gatan DigiScan system. The electron beam was modulated at a 50% duty cycle under all experimental conditions to maximize the amplitude of AC thermal wave. The EDM system supported modulation frequencies up to 500 kHz at 300 kV. In situ thermal measurements were performed using a twin-probe scanning tunneling microscopy (STM) -TEM holder manufactured by "Nanofactory Instruments AB" (as shown in Figure S1) [26–28]. Thermocouple measurements were enabled by chromel and constantan nanoprobes fabricated by electrochemical etching of 200 μm diameter wires [see detailed methods in Ref. [50]. The reference junction temperature for calibration of the thermocouple was the temperature of the Cu jigs holding the probes, which was maintained consistently at ~298 K (room temperature) inside the TEM column. Additionally, previous experiments have shown that the thermocouple temperature returns to a steady state ≤ 500 μs, or less, after spot heating by a focused electron beam [26]. That is, the reference temperature satisfies the requirement that it should not be affected by a temperature increase with respect to the nanosized junction. This rapid relaxation minimizes the influence of residual heating during beam scanning and ensures that the detected temperature modulation primarily reflects the local thermal response. The chromel and constantan probes were independently operated through a piezo-driving system to make direct contact with a specimen. To ensure proper electrical contact, a 100 nA DC current was applied to the thermocouple junction, and the applied voltage was measured. The total impedance of the electrical circuit, including the junction, was maintained below 1 kΩ to detect clear signals of thermal waves. A lock-in amplifier (model SR865A, Stanford Research Systems) was used with an oscilloscope (Keysight InfiniiVision DSOX3034T) to obtain the phase delay and amplitude of thermal waves during the beam scanning. The sensitivity and time constant were optimized to achieve a favorable signal-to-noise ratio while avoiding overloading the system. The dwell time per pixel was set to match or exceed the time constant to avoid shifting of the map of phase delay or amplitude in relation to the HAADF-STEM image. In addition, noise filters and differential amplifiers were used to remove unwanted noise and enhance desired signals, respectively. Since the specimen stage can slowly drift over time, the total exposure time per measurement was limited to <2 h to avoid the deformation of phase delay/amplitude maps.

Acknowledgments

This research was supported by JST Mirai Program, Japan (grant number JPMJMI19A1) and JST PRESTO, Japan, Grant Number JPMJPR24J4. This work was also supported by "Advanced Research Infrastructure

for Materials and Nanotechnology in Japan (ARIM)" of the Ministry of Education, Culture, Sports, Science and Technology (MEXT). Proposal Number JPMXP1224NM5382.

Conflicts of Interest

The authors declare no conflicts of interest.

Data Availability Statement

The data that support the findings of this study are available from the corresponding author upon reasonable request.

References

1. S. Srivastava, A. Jaiswal, and A. Khan, *Semiconductor Nanoscale Devices: Materials and Design Challenges* (Bentham Science Publishers, 2025), 1–26.

2. J. Liu, H. Wang, Y. Hu, W. Ma, and X. Zhang, "Laser Flash-Raman Spectroscopy Method for the Measurement of the Thermal Properties of Micro/Nano Wires," *Review of Scientific Instruments* 86 (2015): 014901, https://doi.org/10.1063/1.4904868.

3. C. Li, S. Xu, Y. Yue, B. Yang, and X. Wang, "Thermal Characterization of Carbon Nanotube fiber by Time-Domain Differential Raman," *Carbon* 103 (2016): 101–108, https://doi.org/10.1016/j.carbon.2016.03.003.

4. R. Anufriev, "Measurement of the Phonon Mean Free Path Spectrum in Silicon Membranes at Different Temperatures Using Arrays of Nanoslits," *Physical Review B* 101 (2020): 115301, https://doi.org/10.1103/PhysRevB.101.115301.

5. A. Sood, R. Cheaito, T. Bai, et al., "Direct Visualization of Thermal Conductivity Suppression due to Enhanced Phonon Scattering near Individual Grain Boundaries," *Nano Letters* 18 (2018): 3466–3472, https://doi.org/10.1021/acs.nanolett.8b00534.

6. E. Isotta, S. Jiang, R. Bueno-Villoro, et al., "Heat Transport at Silicon Grain Boundaries," *Advanced Functional Materials* 34 (2024): 2405413, https://doi.org/10.1002/adfm.202405413.

7. E. Isotta, S. Jiang, G. Moller, A. Zevalkink, G. J. Snyder, and O. Balogun, "Microscale Imaging of Thermal Conductivity Suppression at Grain Boundaries," *Advanced Materials* 35 (2023): 2302777, https://doi.org/10.1002/adma.202302777.

8. M. Feldman, C. Vernier, R. Nag, et al., "Anisotropic Thermal Transport in Tunable Self-Assembled Nanocrystal Supercrystals," *ACS Nano* 18 (2024): 34341–34352, https://doi.org/10.1021/acsnano.4c12991.

9. T. Baba, T. Baba, and T. Mori, "Development of Fourier Transform Ultrafast Laser Flash Method for Simultaneous Measurement of Thermal Diffusivity and Interfacial Thermal Resistance," *International Journal of Thermophysics* 45 (2024): 27, https://doi.org/10.1007/s10765-023-03324-w.

10. T. Baba, T. Baba, and T. Mori, "Fourier Transform Thermoreflectance Method Under Front-Heat Front-Detect Configuration," *International Journal of Thermophysics* 45 (2024): 61, https://doi.org/10.1007/s10765-024-03351-1.

11. D. Alikin, M. J. Pereira, A. Abramov, et al., "Nanoscale Imaging and Measurements of Grain Boundary Thermal Resistance in Ceramics with Scanning Thermal Wave Microscopy," *ACS Applied Materials & Interfaces* 16 (2024): 42917–42930, https://doi.org/10.1021/acsami.4c08085.

12. K. Kim, W. Jeong, W. Lee, and P. Reddy, "Ultra-High Vacuum Scanning Thermal Microscopy for Nanometer Resolution Quantitative Thermometry," *ACS Nano* 6 (2012): 4248–4257, https://doi.org/10.1021/nn300774n.

13. F. Menges, P. Mensch, H. Schmid, H. Riel, A. Stemmer, and B. Gotsmann, "Temperature Mapping of Operating Nanoscale Devices by Scanning Probe Thermometry," *Nature Communications* 7 (2016): 10874, https://doi.org/10.1038/ncomms10874.

14. S. Gonzalez-Munoz, K. Agarwal, E. G. Castanon, et al., "Direct Measurements of Anisotropic Thermal Transport in γ-InSe Nanolayers via Cross-Sectional Scanning Thermal Microscopy," *Advanced Materials Interfaces* 10 (2023): 2300081, https://doi.org/10.1002/admi.202300081.

15. D. Seto, R. Nikka, S. Nishio, Y. Taguchi, T. Saiki, and Y. Nagasaka, "Nanoscale Optical Thermometry Using a Time-correlated Single-photon Counting in an Illumination-collection Mode," *Applied Physics Letters* 110 (2017): 033109, https://doi.org/10.1063/1.4974451.

16. Q. Weng, K.-T. Lin, K. Yoshida, et al., "Near-Field Radiative Nanothermal Imaging of Nonuniform Joule Heating in Narrow Metal Wires," *Nano Letters* 18 (2018): 4220–4225, https://doi.org/10.1021/acs.nanolett.8b01178.

17. H. Guo, M. I. Khan, C. Cheng, et al., "Vanadium Dioxide Nanowire-based Microthermometer for Quantitative Evaluation of Electron Beam Heating," *Nature Communications* 5 (2014): 4986, https://doi.org/10.1038/ncomms5986.

18. L. Shi, L. He, L. Shangguan, et al., "Revealing the Phase Segregation and Evolution Dynamics in Binary Nanoalloys via Electron Beam-assisted Ultrafast Heating and Cooling," *ACS Nano* 16 (2022): 921.

19. P.-I. Wang, Y.-P. Zhao, G.-C. Wang, and T.-M. Lu, "Novel Growth Mechanism of Single Crystalline Cu Nanorods by Electron Beam Irradiation," *Nanotechnology* 15 (2003): 218–222, https://doi.org/10.1088/0957-4484/15/1/039.

20. C. A. Gadre, X. Yan, Q. Song, et al., "Nanoscale Imaging of Phonon Dynamics by Electron Microscopy," *Nature* 606 (2022): 292–297, https://doi.org/10.1038/s41586-022-04736-8.

21. J. Kikkawa, "Optical and Acoustic Phonon Temperature Measurements Using Electron Nanoprobe and Electron Energy Loss Spectroscopy," *Physical Review B* 106 (2022): 195431, https://doi.org/10.1103/PhysRevB.106.195431.

22. J. C. Idrobo, "Temperature Measurement by a Nanoscale Electron Probe Using Energy Gain and Loss Spectroscopy," *Physical Review Letters* 120 (2018): 095901, https://doi.org/10.1103/PhysRevLett.120.095901.

23. M. J. Lagos and P. E. Batson, "Thermometry with Subnanometer Resolution in the Electron Microscope Using the Principle of Detailed Balancing," *Nano Letters* 18 (2018): 4556–4563, https://doi.org/10.1021/acs.nanolett.8b01791.

24. X. Yan, C. Liu, C. A. Gadre, et al., "Unexpected Strong Thermally Induced Phonon Energy Shift for Mapping Local Temperature," *Nano Letters* 19 (2019): 7494–7502, https://doi.org/10.1021/acs.nanolett.9b03307.

25. M. Mecklenburg, W. A. Hubbard, E. R. White, et al., "Nanoscale Temperature Mapping in Operating Microelectronic Devices," *Science* 347 (2015): 629–632, https://doi.org/10.1126/science.aaa2433.

26. N. Kawamoto, Y. Kakefuda, I. Yamada, et al., "Visualizing Nanoscale Heat Pathways," *Nano Energy* 52 (2018): 323–328, https://doi.org/10.1016/j.nanoen.2018.08.002.

27. N. Kawamoto, Y. Kakefuda, T. Mori, et al., "Nanoscale Characterization of the Thermal Interface Resistance of a Heat-Sink Composite Material by in Situ TEM," *Nanotechnology* 26 (2015): 465705, https://doi.org/10.1088/0957-4484/26/46/465705.

28. H. D. Nguyen, I. Yamada, T. Nishimura, et al., "STEM in Situ Thermal Wave Observations for Investigating Thermal Diffusivity in Nanoscale Materials and Devices," *Science Advances* 10 (2024): eadj3825, https://doi.org/10.1126/sciadv.adj3825.

29. R. McKinney, P. Gorai, E. S. Toberer, and V. Stevanovic`, "Rapid Prediction of Anisotropic Lattice Thermal Conductivity: Application to Layered Materials," *Chemistry of Materials* 31 (2019): 2048–2057, https://doi.org/10.1021/acs.chemmater.8b05084.

30. R. R. Monchamp, "Preparation and Properties of Crystalline Laser Oxide Materials," *Journal of Solid State Chemistry* 12 (1975): 201–206, https://doi.org/10.1016/0022-4596(75)90306-0.

31. A. J. Angström, "The London, Edinburgh, and Dublin Philosophical Magazine," *Journal of Science* 25 (1863): 130.

32. J. Morikawa and T. Hashimoto, "Analysis of High-Order Harmonics of Temperature Wave for Fourier Transform Thermal Analysis," *Japanese Journal of Applied Physics* 37 (1998): L1484, https://doi.org/10.1143/JJAP.37.L1484.

33. H. Cho, S. Y. Back, J. H. Yun, S. Byeon, H. Jin, and J.-S. Rhyee, "Thermoelectric Properties and Low-Energy Carrier Filtering by Mo Microparticle Dispersion in an n-Type $(CuI)_{0.003}$ Bi_2 $(Te,Se)_3$ Bulk Matrix," *ACS Applied Materials & Interfaces* 12 (2020): 38076–38084, https://doi.org/10.1021/acsami.0c09529.

34. H. Cho, J.-H. Yun, S. Y. Back, et al., "Superior Thermoelectric Cooling Performance by Suppressing Bipolar Diffusion Effect and Enhancing Anisotropic Texture in p-/n-type Bi_2Te_3 Based Compounds," *Journal of Alloys and Compounds* 888 (2021): 161572, https://doi.org/10.1016/j.jallcom.2021.161572.

35. I. T. Witting, T. C. Chasapis, F. Ricci, et al., "The Thermoelectric Properties of Bismuth Telluride," *Advanced Electronic Materials* 5 (2019): 1800904, https://doi.org/10.1002/aelm.201800904.

36. G. Chen, "Non-Fourier Phonon Heat Conduction at the Microscale and Nanoscale," *Nature Reviews Physics* 3 (2021): 555–569, https://doi.org/10.1038/s42254-021-00334-1.

37. C. Hua, "Transport Regimes in Quasiballistic Heat Conduction," *Physical Review B* 89 (2014): 094302, https://doi.org/10.1103/PhysRevB.89.094302.

38. M. L. Shendeleva, "Thermal Wave Reflection and Refraction at a Plane Interface: Two-Dimensional Geometry," *Physical Review B* 65 (2002): 134209, https://doi.org/10.1103/PhysRevB.65.134209.

39. V. R. Li, G. Liakhou, S. Paoloni, C. Sibilia, and M. Bertolotti, "Thermal Waves Physics," *Journal of Optoelectronics and Advanced Materials* 3 (2001): 779–816.

40. A. Jacquot, N. Farag, M. Jaegle, et al., "Thermoelectric Properties as a Function of Electronic Band Structure and Microstructure of Textured Materials," *Journal of Electronic Materials* 39 (2010): 1861–1868, https://doi.org/10.1007/s11664-009-1059-x.

41. H. J. Goldsmid, "Recent Studies of Bismuth Telluride and Its Alloys," *Journal of Applied Physics* 32 (1961): 2198–2202, https://doi.org/10.1063/1.1777042.

42. D. G. Cahill, W. K. Ford, K. E. Goodson, et al., "Nanoscale Thermal Transport," *Journal of Applied Physics* 93 (2003): 793–818, https://doi.org/10.1063/1.1524305.

43. M. M. Rojo, B. Abad, C. V. Manzano, et al., "ow Size Affects Phonon Scattering," *Nanoscale* 9 (2017): 6741–6747, https://doi.org/10.1039/C7NR02173A.

44. Y. Chen, C. Deng, Y. Wei, et al., "Thickness Dependent Anisotropy of in-plane Raman Modes under Different Temperatures in Supported Few-layer WTe_2," *Applied Physics Letters* 119 (2021): 063104, https://doi.org/10.1063/5.0058438.

45. Y. Dong, B.-Y. Cao, and Z.-Y. Guo, "Ballistic–diffusive Phonon Transport and Size Induced Anisotropy of Thermal Conductivity of Silicon Nanofilms Physica E: Low-dimensional Systems and Nanostructures," *Low-dimensional Systems and Nanostructures* 66 (2015): 1–6, https://doi.org/10.1016/j.physe.2014.09.011.

46. S. Huang, M. Segovia, X. Yang, et al., "Anisotropic Thermal Conductivity in 2D Tellurium," *2D Materials* 7 (2019): 015008.

47. B. Dongre, J. Carrete, N. Mingo, and G. K. H. Madsen, "Ab Initio Lattice Thermal Conductivity of Bulk and Thin-Film α-AI_2O_3," *MRS Communications* 8 (2018): 1119–1123, https://doi.org/10.1557/mrc.2018.161.

48. L. Chen, W. Zhang, H. Zhang, et al., "In-Plane Anisotropic Thermal Conductivity of Low-Symmetry $PdSe_2$," *Sustainability* 13 (2021): 4155, https://doi.org/10.3390/su13084155.

49. M. Muñoz Rojo, S. Grauby, J.-M. Rampnoux, O. Caballero-Calero, M. Martin-Gonzalez, and S. Dilhaire, "Fabrication of Bi_2Te_3 Nanowire Arrays and Thermal Conductivity Measurement by 3ω-Scanning Thermal Microscopy," *Journal of Applied Physics* 113 (2013): 054308, https://doi.org/10.1063/1.4790363.

50. Y. Kakefuda, N. Kawamoto, M. Mitome, I. Yamada, T. Mori, and D. Golberg, "Development of Nanoscale Thermocouple Probes for Local Thermal Measurements," *e-Journal of Surface Science and Nanotechnology* 17 (2019): 102–107, https://doi.org/10.1380/ejssnt.2019.102.

Supporting Information

Additional supporting information can be found online in the Supporting Information section.

Supporting File: apxr70144-sup-0001-SuppMat.docx.